A Generalized Split-Window Algorithm for Retrieving Land-Surface Temperature from Space

Zhengming Wan and Jeff Dozier, *Associate Member, IEEE*

Abstract—**We propose a generalized split-window method for retrieving land-surface temperature (LST) from AVHRR and MODIS data. Accurate radiative transfer simulations show that the coefficients in the split-window algorithm for LST must vary with the viewing angle, if we are to achieve a LST accuracy of about 1 K for the whole scan swath range (±55° from nadir) and for the ranges of surface temperature and atmospheric conditions over land, which are much wider than those over oceans. We obtain these coefficients from regression analysis of radiative transfer simulations, and we analyze sensitivity and error over wide ranges of surface temperature and emissivity and atmospheric water vapor abundance and temperature. Simulations show that when atmospheric water vapor increases and viewing angle is larger than 45°, it is necessary to optimize the split-window method by separating the ranges of the atmospheric water vapor, lower boundary temperature, and the surface temperature into tractable subranges. The atmospheric lower boundary temperature and (vertical) column water vapor values retrieved from HIRS/2 or MODIS atmospheric sounding channels can be used to determine the range for the optimum coefficients of the split-window method. This new algorithm not only retrieves land-surface temperature more accurately, but is also less sensitive to uncertainty in emissivity and to instrument quantization error.**

I. Introduction

LAND-SURFACE temperature (LST) is one of the key parameters in the physics of land-surface processes on regional and global scales, combining the results of all surface-atmosphere interactions and energy fluxes between the atmosphere and the ground [1], [2]. Therefore, it is required for a wide variety of climatic, hydrological, ecological, and biogeochemical studies [3], [4]. For example, canopy temperature can be used to estimate sensible heat flux [5]; soil-surface temperature can be used to estimate sensible and latent heat fluxes [6]; and satellite-measured surface temperature can be used to improve models and methods for evaluating land-surface energy balance [7]. Global climate model (GCM) simulations indicate that stronger summer monsoons are associated with higher land temperatures [8]. The canopy temperature may be also used to evaluate water requirements of wheat [9] and to determine frosts in orange groves [10]. In order to understand the entire Earth system better on the global scale, the Earth Observing System (EOS) will provide surface kinetic temperatures at specified accuracies of 0.3 K for oceans and 1 K over land. The international Tropical Ocean Global Atmosphere (TOGA) program has specified that sea surface temperature (SST) should be accurate to 0.3 K for global numerical models of climate.

Manuscript received February 16, 1995; revised February 2, 1996. This work was supported by the EOS Program under Contract NAS5-31370 and the HPCC Program under Award NAG5-2485 of the National Aeronautics and Space Administration.

The authors are with the Institute for Computational Earth System Science, University of California, Santa Barbara, CA 93106-3060 USA.

Publisher Item Identifier S 0196-2892(96)03638-8.

A. Infrared Measurement of Surface Temperature

During the past decade, significant progress has been made in estimation of land-surface emissivity and temperature from airborne thermal infrared data. Kahle *et al.* [11] developed a technique to estimate the surface temperature based on an assumed constant emissivity in one channel and previously determined atmospheric parameters and then estimate the emissivity in other channels [12]. Other techniques, such as thermal log residuals and alpha residuals, have been recently developed to extract emissivity information from multispectral thermal infrared data [13].

Two types of methods have been developed to estimate LST from space: the single infrared channel method and the split-window method. The single-channel method requires a good radiative transfer model and atmospheric profiles, which must be given by either satellite soundings or conventional radiosonde [14], [15].

The split-window method corrects for atmospheric effects based on the differential absorption in adjacent infrared bands [16]–[24]. Li and Becker [25] proposed a method to estimate both land-surface emissivity and LST using pairs of day/night co-registered AVHRR images. They use a temperature-independent spectral index (TISI) in thermal infrared bands and assume knowledge of surface TIR BRDF (bidirectional reflectance distribution function) and atmospheric profiles.

Recent progress in SST algorithms [26]–[28] also provides useful information for the development of LST algorithms. Sobrino *et al.* [28] show that including column water vapor in the split-window algorithm improves SST accuracy.

Because of the difficulties in correcting for atmospheric absorption, atmospheric emission, and surface emissivity, the development of accurate LST algorithms is not easy. The accuracy of atmospheric corrections is limited by radiative transfer methods, uncertainties in atmospheric molecular absorption coefficients (especially water vapor) and aerosol absorption/scattering coefficients, and uncertainties in atmospheric profiles. Atmospheric transmittance/radiance codes LOWTRAN6 [29], LOWTRAN7 [30], and MODTRAN [31] have been widely used in development of SST and LST algorithms. A common method used for calculation of radiative flux in these codes is the two-stream approximation. A single scattering approximation is used in LOWTRAN6,

while a three-term K-distribution multiple scattering parameterization is used in LOWTRAN7, and a multiple scattering approximation without K-distribution is used in MODTRAN. The newest version of MODTRAN uses the discrete-ordinates method [32]. Other different approximations in these codes include the Curtis–Godson approximation, Beer's law to calculate optical depth (although atmospheric transmission does not obey Beer's law), and omitting absorption overlap. Quantitative comparisons between these codes indicate that the approximations are accurate within 0.5–2% in the 3.4–4.1 μm, and 8–13 μm atmospheric windows. Moreover, TIR band transmittance may differ by 6% within these windows and by more than 30% near the edges of these windows due to different molecular band absorption models used in LOWTRAN7 and MODTRAN [33]. A review for measurements of water vapor absorption in the 8–13 μm atmospheric window over the past 20 years reveals considerable variation in its magnitude [34]. The accuracy of water vapor continuum absorption in five of the measurements reviewed is about 10%, adequate experimental measurements are lacking at temperatures below 280 K. Recent theoretical studies [35], [36] on water vapor continuum absorption reveal that the empirical model [37], widely used in transmission codes, fails to satisfy the principle of detailed balance that governs the emission and absorption processes. These theoretical studies have also led to significant progress in understanding the physical mechanisms and in the ability to predict their magnitude and temperature dependence. Barton [38] explored the possibility to derive water vapor absorption coefficients from satellite TIR data.

B. Microwave Measurement of Surface Temperature

Thermal infrared remote sensing can retrieve LST only in clear-sky conditions. Microwave techniques have the great advantage of having an all-weather capability. McFarland *et al.* [39] derived surface temperature over crop/range, moist soils, and dry soils areas in the Central Plains of the United States from the MDSP Special Sensor Microwave/Imager data. A regression analysis between all SSM/I channels and minimum screen air temperatures (representing the surface temperatures) showed correlations with rms errors of about 3°C. They also found that snow-surface temperature retrieval is very difficult, if not impossible, because snow's emissivity varies with depth, density, and grain size, and that land surfaces with large areas of water present, such as lakes and flooded soils, also present problems because of the integrated influence of the much lower brightness temperatures and higher polarization differences for water. The presence of falling rain masks the radiation emitted from the surface. Microwave remote sensing has been better used to retrieve soil moisture [40]–[42] because of the large contrast between the dielectric constant of water and that of dry soil. In the microwave range, soil emissivities vary from 0.6 for wet soil (≈30% volumetric soil moisture) to 0.9 for dry soil (≈8%) [43]. Although satellite-borne microwave radiometers have been providing information about atmospheric and oceanic parameters for several years, they have not provided land parameters, with the exception of snow monitoring, because 1) the spatial resolution of the satellite radiometers flown to date is more compatible with the dimensions associated with the spatial variations of most atmospheric and oceanic parameters than with those of most land parameters and 2) the mechanisms responsible for microwave emission from land surfaces and volumes are not well understood, in part because land targets generally have complicated dielectric and geometric properties.

C. MODIS (Moderate Resolution Imaging Spectroradiometer)

MODIS is an EOS instrument that will serve as the keystone [44] for global studies of atmosphere [45], land [4], and ocean processes. It scans ±55° from nadir in 36 bands, with bands 1–19 and band 26 in the visible and near infrared range, and the remaining bands in the thermal infrared from 3–15 μm. It will provide images of daylight reflection and day/night emission of the Earth every 1–2 days, with continuous duty cycle. It uses 12 bits for quantization in all bands. The thermal infrared bands have an IFOV (instantaneous field-of-view) of about 1 km at nadir. MODIS will view cold space and a full-aperture blackbody before and after viewing the Earth scene in order to achieve calibration accuracy of better than 1% absolute for thermal infrared bands. MODIS is particularly useful because of its global coverage, radiometric resolution and dynamic ranges, and accurate calibration in multiple thermal infrared bands designed for retrievals of SST, LST and atmospheric properties. Specifically, bands 3–7, 13, and 16–19 will be used to classify land-cover to infer emissivities, band 26 will detect cirrus clouds, and thermal infrared bands 20, 22, 23, 29, 31, and 32 correct for atmospheric effects and retrieve surface emissivity and temperature. The atmospheric sounding channels of MODIS retrieve atmospheric temperature and water vapor profiles. Multiple bands in the mid-infrared range will provide, for the first time, corrections for solar radiation in daytime LST estimations using mid-infrared data. Table I shows the wavelength ranges for AVHRR and MODIS.

II. Background on Land-Surface Emissivities

For an uniform surface at surface temperature T_s, we can define its band average emissivity by spectral emissivity $\varepsilon(\lambda)$ and the spectral response function of the sensor in this band, $\Psi(\lambda)$, in a way similar to the definition of spectral emissivity:

$$\overline{\varepsilon} = \frac{\int_{\lambda_1}^{\lambda_2} \Psi(\lambda)\varepsilon(\lambda)\mathrm{B}(\lambda, T_s)\, d\lambda}{\int_{\lambda_1}^{\lambda_2} \Psi(\lambda)\mathrm{B}(\lambda, T_s)\, d\lambda}. \tag{1}$$

This band-averaged emissivity is a function of the surface temperature. λ_1 and λ_2 are lower and upper boundaries of the band, and B is the Planck function. In Earth's environment, this temperature-dependence is usually very small. In an extreme example of coarse sands [46], the spectral emissivity increases from 0.667 at 3.5 μm to 0.907 at 4.25 μm in the medium wavelength range where AVHRR channel 3 is located. Its band-average emissivity changes only 0.004 as the temperature changes from 240 to 320 K. Therefore,

the Planck function term $B(\lambda, T)$ in (1) can be omitted without introducing any significant error, and the band-average emissivity can be calculated from spectral emissivity values.

How to define the band-average emissivity for mixed pixels is not so obvious. If a pixel consists of two land covers, one with emissivity ε_1 and surface temperature T_1, the other with ε_2 and T_2, and proportions are p_1 and p_2, there are two ways to define its band-average emissivity. The first one simply extends (1) to the mixed pixel. The average emissivity in band i will be

$$\overline{\varepsilon_i} = \frac{\int_{\lambda(i,\,\text{lower})}^{\lambda(i,\,\text{upper})} \Psi(\lambda)[p_1\varepsilon_1(\lambda)\,B(\lambda, T_1) + p_2\varepsilon_2(\lambda)\,B(\lambda, T_2)]\,d\lambda}{\int_{\lambda(i,\,\text{lower})}^{\lambda(i,\,\text{upper})} \Psi(\lambda)\,[p_1 B(\lambda, T_1) + p_2 B(\lambda, T_2)]\,d\lambda} \tag{2}$$

where $\lambda(i,\,\text{lower})$ and $\lambda(i,\,\text{upper})$ are lower and upper boundaries of band i, and the denominator defines the numerical value of the effective Planck function of the mixed pixel as if its components are all blackbodies. The second way is to define a temperature-independent band-average emissivity as long as other physical properties of the surface do not change as its temperature changes

$$\overline{\varepsilon_i} = \frac{\int_{\lambda(i,\,\text{lower})}^{\lambda(i,\,\text{upper})} \Psi(\lambda)[p_1\varepsilon_1(\lambda) + p_2\varepsilon_2(\lambda)]\,d\lambda}{\int_{\lambda(i,\,\text{lower})}^{\lambda(i,\,\text{upper})} \Psi(\lambda)\,d\lambda}. \tag{3}$$

Correspondingly, the numerical value of the effective Planck function of the mixed pixel in band i is

$$\overline{B_i}[T_s(i)] = \frac{\int_{\lambda(i,\,\text{lower})}^{\lambda(i,\,\text{upper})} \Psi(\lambda)[p_1\varepsilon_1(\lambda)\,B(\lambda, T_1) + p_2\varepsilon_2(\lambda)\,B(\lambda, T_2)]\,d\lambda}{\int_{\lambda(i,\,\text{lower})}^{\lambda(i,\,\text{upper})} \Psi(\lambda)\,[p_1\varepsilon_1(\lambda) + p_2\varepsilon_2(\lambda)]\,d\lambda} \tag{4}$$

where $T_s(i)$ is the effective radiometric surface temperature in band i.

We show some numerical results for mixed pixels with two components, sandy soil and grass, in Table II, where the band-average emissivity defined by (2) is in the first part and that defined by (3) in the second part. The spectral emissivities of these two materials are calculated from the reflectance spectra labeled as soil sample 0145 and grass sample indiang in Salisbury and D'Aria's paper [47], where spectra were plotted only in the 8–14 μm range. The spectral response functions for NOAA-11 AVHRR bands 3, 4, and 5, and the specified response functions for MODIS bands 29, 31, and 32 are used in the calculations. We considered 6 different cases: a) only one component of sandy soil at 300 K; b) only one component of grass at 300 K; c) equal proportions of sandy soil and grass at 300 K; d) and e) equal proportions of sandy soil and grass at different temperatures; and f) equal proportions of grass at 300 and 285 K. In real situations, the temperature of vegetation canopies is usually lower than soil temperature and surface temperature under shadows is lower than in sunshine areas. The temperature difference is typically 10–20 K. Numerical simulations indicate that the band-average emissivity defined by (2) works well only in isothermal cases A, B, and C, and in single material case, F. For case F, the same material with proportions at different temperatures, the two average emissivities defined by (2) and (3) are almost the same. In the general mixing cases D and E, emissivity varies not only with the proportions but also with temperatures T_1 and T_2. The band emissivity defined by (3) is more accurate because it does not vary with subpixel temperatures. However, even using (3) to define the band emissivity, the effective band temperature defined by (4) varies with band because the Planck function increases with temperature at a higher rate at shorter wavelength and the mixing effect also varies with band. The effective band temperature in AVHRR band 3 may be different from the values in the split-window bands by up to 0.5 K, and the band temperature difference for MODIS band 29 (8.4–8.7 μm) may be up to 0.35 K in the extreme case D. However, the band temperature difference between split-window bands is very small. It is less than 0.1 K for AVHRR bands 4 and 5. It does not exceed 0.04 K for MODIS bands 31 and 32 because these two bands are narrower. This value is less than the noise-equivalent temperature difference (NEΔT), 0.05 K, specified for MODIS bands 31 and 32. This means that the thermal emittance from mixed pixels can be expressed by a temperature-independent band emissivity defined by (3) and a single surface radiometric temperature only in the split-window spectral region. Special care should be taken for the mixing effect in shorter-wavelength regions.

From the point of view of satellite remote sensing, the land surface is the top layer of the interface between the lower boundary of the atmosphere and the solid Earth. In the thermal infrared region, this top layer is a few millimeters thick. The Earth's land surface consists of evergreen forest and shrubs, deciduous forest and shrubs, crop and grass lands, inland water bodies, wetlands, ice or snow, barren and urban areas, bare soil, exposed bedrock, volcanic rocks, sands, shale, and sediments. One of the major difficulties in development of LST algorithms is the considerable spectral variation in emissivities for these different materials. For many of them, emissivities have been measured only for the spectrally integrated range from 8–14 μm [47]–[50]. Emissivity may also vary with the viewing angle [51]–[53], an effect that is more important over land than over water because the combination of surface slope and sensor scan angle routinely results in local viewing angles near 70°. In laboratory measurements of bare soils, Labed and Stoll [52] showed that this angular effect is smaller at wavelengths 10.6 and 12.0 μm than at 3.7 μm. Oblique viewing results in reducing of the signature, the spectral features being essentially unchanged. At viewing angle 60°, this angular effect does not exceed 1.5% for sand and silty materials but it is about 5% for agricultural soils. Soil emissivity may vary with soil particle size [54], and atmospheric effects may cause the emissivity spectra derived from field measurement and airborne sensor data to differ

TABLE I
THE WAVELENGTH RANGES FOR NOAA-11 AVHRR AND MODIS BANDS. THE RANGE IS DEFINED BY ITS LOWER AND UPPER EDGES WHERE THE RESPONSE IS HALF OF THE PEAK RESPONSE

AVHRR band			MODIS band		
no.	lower band edge (μm)	upper band edge (μm)	no.	lower band edge (μm)	upper band edge (μm)
1	0.572	0.697	1	0.620	0.670
2	0.716	0.986	2	0.841	0.876
			3	0.459	0.479
			4	0.545	0.565
			5	1.230	1.250
			6	1.628	1.652
			7	2.105	2.155
			8	0.405	0.420
			9	0.438	0.448
			10	0.483	0.493
			11	0.526	0.536
			12	0.546	0.556
			13	0.662	0.672
			14	0.673	0.683
			15	0.743	0.753
			16	0.862	0.877
			17	0.890	0.920
			18	0.931	0.941
			19	0.915	0.965
3	3.54	3.94	20	3.660	3.840
			21	3.929	3.989
			22	3.929	3.989
			23	4.020	4.080
			24	4.433	4.498
			25	4.482	4.549
			26	1.360	1.390
			27	6.535	6.895
			28	7.175	7.475
			29	8.400	8.700
4	10.32	11.32	31	10.780	11.280
5	11.41	12.38	32	11.770	12.270
			33	13.185	13.485
			34	13.485	13.785
			35	13.785	14.085
			36	14.085	14.385

from the spectra derived from laboratory data [55]. Accurate determination of surface emissivity requires information about the surface BRDF. The conventional method of measuring surface emissivity with an integrating sphere assumes that the reference surface and a sample surface have a similar BRDF. Otherwise, the uncertainty in measured emissivity may be ±5% in cases of mixed diffuse and nondiffuse samples and [56] if an appropriate baffle is not configurated in the intergrating sphere. In vegetation, the emitted radiance also varies with the viewing angle because of temperature structure in the vegetation canopy [57].

Despite all these variations, spectral emissivity characteristics for terrestrial land covers are relatively stable in the wavelength range 10.5–12.5 μm, where AVHRR bands 4 and 5 and MODIS bands 31 and 32 are located. Moreover, spectral contrast in surface emissivities usually decreases with aggregation as spatial scale increases. Salisbury and D'Aria [47] published spectral reflectance data of 79 pure terrestrial materials including igneous, metamorphic, and sedimentary rocks, varnished rock surfaces, lichen-covered sandstone, soil samples, green foliage, senescent foliage, ice, and water surfaces with suspended quartz sediment and oil slicks. The average emissivities in NOAA-11 AVHRR bands 4 and 5 calculated from these reflectance spectra are shown in Fig. 1.

In Fig. 1, the solid line represents the grey body relation $\overline{\varepsilon_4} = \overline{\varepsilon_5}$ and the upper and lower dashed lines represent $\overline{\varepsilon_5} - \overline{\varepsilon_4} = 0.023$ and $\overline{\varepsilon_5} - \overline{\varepsilon_4} = -0.015$. We can gain the following insights into the band-average emissivities of terrestrial materials in the available database: 1) all $\overline{\varepsilon_4}$ and $\overline{\varepsilon_5}$ are larger than 0.825; 2) a general relation $-0.015 \leq \overline{\varepsilon_5} - \overline{\varepsilon_4} \leq 0.023$ holds for all samples except fresh rocks, smooth distilled water ice, and senescent beech foliage; and 3) $\overline{\varepsilon_4}$ and $\overline{\varepsilon_5}$ are larger than 0.91 for all samples except fresh rock and senescent leaves. Salisbury and D'Aria [47] also point out that multiple scattering within the vegetation canopy will reduce spectral contrast and that typical trees, bushes, and grass have emissivities quite close to 1. Field measurements of prairie grasses have shown a spectral emis-

TABLE II

THE BAND EMISSIVITIES AND EFFECTIVE TEMPERATURES OF A PIXEL MIXED WITH TWO COMPONENTS (SANDY SOIL AND GRASS) IN NOAA-11 AVHRR AND EOS MODIS BANDS FOR 6 CASES. THE FIRST PART IS FOR BAND EMISSIVITIES DEFINED BY (2) AND THE SECOND FOR THOSE DEFINED BY (3). TWO ROWS ARE LISTED FOR EACH CASE. THE FIRST ROW GIVES PROPORTION p_i AND SURFACE TEMPERATURE T_s FOR TWO COMPONENTS FOLLOWED BY BAND EMISSIVITIES FOR AVHRR BANDS AND MODIS BANDS. THE SECOND ROW GIVES NAMES OF TWO COMPONENTS FOLLOWED BY BAND RADIOMETRIC TEMPERATURES FOR AVHRR AND MODIS BANDS

Case	pixel mixing parameters				AVHRR band			MODIS band		
					$\overline{\varepsilon_3}\|T_s(3)$	$\overline{\varepsilon_4}\|T_s(4)$	$\overline{\varepsilon_5}\|T_s(5)$	$\overline{\varepsilon_{29}}\|T_s(29)$	$\overline{\varepsilon_{31}}\|T_s(31)$	$\overline{\varepsilon_{32}}\|T_s(32)$
	p_1	T_1	p_2	T_2	3.54-3.94 μm	10.32-11.32 μm	10.41-12.38 μm	8.4-8.7 μm	10.78-11.28 μm	11.77-12.27 μm
band emissivities defined by (2)										
A	1.0	300 °K	0.0	300 °K	0.720	0.953	0.970	0.861	0.955	0.976
	sandy soil		grass		300.00 °K	300.00 °K	300.00 °K	300.00 °K	300.00 °K	300.00 °K
B	0.0	300 °K	1.0	300 °K	0.967	0.962	0.976	0.977	0.966	0.978
	sandy soil		grass		300.00 °K	300.00 °K	300.00 °K	300.00 °K	300.00 °K	300.00 °K
C	0.5	300 °K	0.5	300 °K	0.844	0.958	0.973	0.919	0.960	0.977
	sandy soil		grass		300.00 °K	300.00 °K	300.00 °K	300.00 °K	300.00 °K	300.00 °K
D	0.5	300 °K	0.5	275 °K	0.779	0.957	0.972	0.904	0.960	0.977
	sandy soil		grass		290.43 °K	288.24 °K	288.14 °K	288.55 °K	288.21 °K	288.12 °K
E	0.5	300 °K	0.5	285 °K	0.804	0.957	0.973	0.910	0.960	0.977
	sandy soil		grass		293.55 °K	292.76 °K	292.72 °K	292.86 °K	292.75 °K	292.71 °K
F	0.5	300 °K	0.5	285 °K	0.967	0.962	0.976	0.977	0.966	0.978
	grass		grass		293.55 °K	292.76 °K	292.72 °K	292.86 °K	292.75 °K	292.71 °K
band emissivities defined by (3)										
A	1.0	300 °K	0.0	300 °K	0.725	0.953	0.970	0.861	0.955	0.976
	sandy soil		grass		299.85 °K	300.00 °K	299.99 °K	300.01 °K	300.00 °K	299.99 °K
B	0.0	300 °K	1.0	300 °K	0.968	0.962	0.976	0.977	0.966	0.978
	sandy soil		grass		299.98 °K	300.00 °K	300.00 °K	300.00 °K	300.00 °K	300.00 °K
C	0.5	300 °K	0.5	300 °K	0.846	0.958	0.973	0.919	0.961	0.977
	sandy soil		grass		299.93 °K	300.00 °K	299.99 °K	300.00 °K	300.00 °K	300.00 °K
D	0.5	300 °K	0.5	275 °K	0.846	0.958	0.973	0.919	0.961	0.977
	sandy soil		grass		288.62 °K	288.18 °K	288.09 °K	287.77 °K	288.15 °K	288.11 °K
E	0.5	300 °K	0.5	285 °K	0.846	0.958	0.973	0.919	0.961	0.977
	sandy soil		grass		292.38 °K	292.72 °K	292.69 °K	292.39 °K	292.71 °K	292.71 °K
F	0.5	300 °K	0.5	285 °K	0.968	0.962	0.976	0.977	0.966	0.978
	grass		grass		293.53 °K	292.75 °K	292.72 °K	292.86 °K	292.75 °K	292.71 °K

sivity of 0.99 ± 0.01 [58]. From these measurements, a constant emissivity approximation of 0.96–0.98 in AVHRR band 5 appears quite good for all natural land covers except exposed rocks and sands. Although more field measurements are needed to confirm this approximation, it indicates that the band emissivities in AVHRR bands 4 and 5 and MODIS bands 31 and 32 are relatively stable and known within about 0.01 for dense evergreen canopies, lake surfaces, ice/snow covers, and most soils. Because their band emissivities are close to the emissivities of water surfaces, the effect of rain is negligible for these land covers.

III. RADIATIVE TRANSFER SIMULATIONS

A. Theoretical Method

A fundamental theoretical description for the LST algorithm development [18] is summarized briefly here. Emitted spectral radiance L at wavelength λ from a surface at thermodynamic temperature T_s is given by multiplying the Planck function by spectral emissivity $\varepsilon(\lambda)$

$$L(\lambda, T) = \varepsilon(\lambda)\mathrm{B}(\lambda, T_s). \tag{5}$$

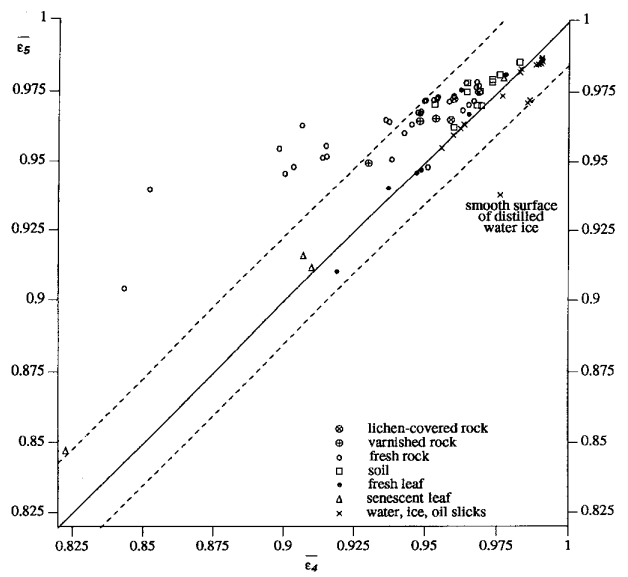

Fig. 1. Band averaged emissivities of terrestrial materials for NOAA-11 AVHRR bands 4 and 5.

In general, azimuthally dependent radiance in an absorbing, emitting, and scattering layer is governed by the monochromatic radiative transfer equation

$$\mu \frac{dL(\tau, \vec{\Omega})}{d\tau} + L(\tau, \vec{\Omega}) = J(\tau, \vec{\Omega}) \tag{6}$$

where τ is optical depth, and $L(\tau, \vec{\Omega})$ is the radiance at level τ along direction $\vec{\Omega}$, which is composed of zenith angle $\arccos \mu$ and azimuth ϕ. The spectral designation is omitted from the equation for simplicity.

The source function J is

$$J(\tau, \vec{\Omega}) = \frac{\tilde{\omega}}{4\pi} \int_{4\pi} P(\tau, \vec{\Omega}; \vec{\Omega}') L(\tau, \vec{\Omega})\, d\Omega' + Q(\tau, \vec{\Omega}) \tag{7}$$

where $P(\tau, \vec{\Omega}; \vec{\Omega}')$ is the scattering phase function. The Q term in (7) represents internal sources. By separating direct from diffuse radiation, it is convenient to consider the radiation scattered from the direct beam or the specularly reflected direct beam as caused by some internal pseudo-source. Then the total internal source is

$$Q(\tau, \vec{\Omega}) = Q_t(\tau, \vec{\Omega}) + Q_s(\tau, \vec{\Omega}) + Q_{sp}(\tau, \vec{\Omega}) \tag{8}$$

where Q_t is the thermal source, and Q_s and Q_{sp} are the direct and specular pseudo-sources.

By applying the interaction principle [59] and doubling/adding method [60], a matrix form of this integro-differential radiative transfer equation can be applied to a vertically inhomogeneous, multilayer atmosphere [61]. The top and bottom boundary conditions that need to be satisfied are that $\mathbf{L}^{\downarrow}(0)$ must be specified (usually zero) and

$$\mathbf{L}^{\uparrow}(\tau_0) = \mathbf{R_g} \mathbf{L}^{\downarrow}(\tau_0) + \vec{\varepsilon} \mathrm{B}(T_s) + \mu_0 E_0 e^{-\tau_0/\mu_0} \mathbf{f_r}(\mu_0). \tag{9}$$

Radiances $\mathbf{L}^{\downarrow\uparrow}$ are vectors of $m \times n$ elements on a discrete angular space composed of m zenith and n azimuth angles. $\mathbf{R_g}$ is the surface diffuse reflection matrix, T_s is the temperature of the surface. $\mathbf{f_r}(\mu_0)$ is the surface BRDF vector to the direct beam, and $\vec{\varepsilon}$ is the emissivity vector.

The directional emissivity and BRDF f_r are coupled by Kirchhoff's law:

$$\varepsilon(\mu) = 1 - \int_0^{2\pi} \int_0^1 \mu' f_r(\mu; \mu', \phi')\, d\mu'\, d\phi'. \tag{10}$$

Numerical results obtained by using the doubling/adding method have been compared with and validated by results obtained by using discrete-ordinate method [32], [62]. The doubling/adding method is used in our radiative transfer simulations due to its advantages in easy implementation of surface interfaces, such as the air-water interface and interfaces for specular reflectance or BRDF reflectance, and in efficiently getting solutions for multiple boundary conditions.

As described thus far, the model is for the monochromatic case only. To make the model work for the atmosphere, we need to know the atmospheric optical properties. Among them the most important are optical thickness τ_0, single scattering albedo $\tilde{\omega}$, and the scattering phase function P, which depend on atmospheric profiles (temperature, pressure, water vapor density, ozone density, and the aerosol density and distribution). LOWTRAN7 [30] and MODTRAN [31] provide absorption band absorption coefficients for calculations of atmospheric molecular transmission functions averaged within wavenumber intervals 5 and 1 cm^{-1}, respectively. This averaging causes violation of the Lambert–Bouguer–Beer law because of the complexity of molecular band absorption even in a narrow wavenumber interval. A solution to this problem is to expand radiative transmission functions calculated from LOWTRAN or MODTRAN by using exponential-sum fitting [63]. The monochromatic radiative transfer model is applied separately to each term in the exponential-sum expansion, and the results are then summed. By solving the radiative transfer equation over the whole wavelength range of a thermal band of a satellite sensor, we get the angular distribution of average spectral radiance:

$$\overline{\mathbf{L}^{\uparrow}} = \frac{\int_{\lambda_1}^{\lambda_2} \Psi(\lambda) \mathbf{L}^{\uparrow}(\lambda, 0)\, d\lambda}{\int_{\lambda_1}^{\lambda_2} \Psi(\lambda)\, d\lambda} \tag{11}$$

where $\mathbf{L}^{\uparrow}(\lambda, 0)$ is the vector of upward spectral radiances at the top of the atmosphere and Ψ is the sensor response function, for the wavelength band whose lower and upper boundaries are $[\lambda_1, \lambda_2]$.

From the theoretical point of view, the success of the LST algorithm depends on 1) accurately dealing with the atmospheric effects; 2) accurately dealing with the surface emissivity effects; and 3) the quality of TIR data including the stability of the spectral response function, signal-to-noise ratio, radiometric resolution, and calibration accuracy. A knowledge base of band emissivities of natural land covers with surface structures at least at small scales is urgently needed. We have started to measure spectral emissivities of natural land materials in laboratory and in fields.

B. Ranges of the Simulations

It is important to make radiative transfer simulations for wide ranges of atmospheric and surface conditions. This is the advantage of the numerical experiments with computers over ground-based measurements that provide data coincident with satellite measurements for establishment of a statistical LST algorithm.

1) *Temperature of the Atmospheric Lower Boundary:* We made radiative transfer simulations for 12 atmospheric temperature profiles, which cover the range of surface air temperatures (T_{air}) from 256–310 K. We plan to extend to 240–325 K in the near future.
2) *Atmospheric Column Water Vapor:* We scaled the water vapor profile from the near saturated level down to 5% of the saturated level for each temperature profile. The (vertical) column water vapor, cwv_v, is mainly limited by the atmospheric lower boundary temperature to a few centimeters in cold conditions and to more than 5 cm in warm tropical conditions.
3) *Surface Temperature:* The land-surface temperature, T_s, ranges from $T_{\text{air}} - 16$ K to $T_{\text{air}} + 16$ K. This range may be extended or reduced if necessary after enough global LST values are retrieved. This wide range will be split into two or more overlapped subranges, for the reason described later.
4) *Land-Surface Emissivities:* Based on available measurement data shown in Fig. 1, we consider surface emissivity variations of natural land covers in two subgroups, one defined by $0.96 \leq \overline{\varepsilon_5} \leq 1.0$ and $-0.025 \leq \overline{\varepsilon_4} - \overline{\varepsilon_5} \leq 0.015$, and another defined by $0.91 \leq \overline{\varepsilon_5} \leq 0.95$ and $-0.025 \leq \overline{\varepsilon_4} - \overline{\varepsilon_5} \leq 0.015$. The first group represents of band emissivity conditions for most land covers. The second group represents some land covers especially at large viewing angles.

C. Computational Simulations

An accurate atmospheric radiative transfer code has been developed for more than ten years on different workstations including IBM RISC/6000, and DEC 3000 Model 800 Alpha workstations. It takes about three hours of CPU time on the DEC 3000/800 Alpha workstation to make a complete simulation for one atmospheric temperature and water vapor condition over the spectral range 775–1000 cm^{-1} with the spectral interval 5 cm^{-1} for a series of surface emissivity and temperature conditions. The exponential-sum tables derived from LOWTRAN-7 transmission functions are used in simulations to obtain results used in this paper. In the spectral range 775–1000 cm^{-1}, the numerical monochromatic radiative transfer equation is solved 1000–8600 times in each spectral interval in order to deal with the molecular band absorptions of H_2O, CO_2, and O_3. Recently, this radiative transfer code has been ported to the CRAY T3D, one of the High Performance Computing and Communications (HPCC) testbeds. The computational time decreases with the number of nodes at an efficiency of 90% on this parallel computing system.

D. Numerical Model of IR Remote Sensing

For given conditions of atmospheric profiles and a land surface, the thermal infrared spectral signature measured from satellite-borne sensors may be expressed as [64]

$$\begin{aligned} L(j) = {} & t_1(j)\varepsilon(j)\,\mathrm{B}(j, T_s) \\ & + \frac{1-\varepsilon(j)}{\pi}\left[t_2(j)\,E_a(j) + t_3(j)\,E_s(j)\right] \\ & + L_a(j) + L_s(j) \end{aligned} \tag{12}$$

where $\varepsilon(j)$ is the band-average emissivity, $t_i(j)$, $i = 1, 2, 3$ are three effective band transmission functions for band j: t_1 for surface thermal emittance, t_2 for atmospheric downward thermal irradiance reflected by the surface, and t_3 for solar irradiance reflected by the surface. L_a is the atmospheric upward thermal radiance, and L_s is path radiance from scattering of solar radiation. In general, these three effective band transmission functions are different because of selective, wavelength-dependent molecular band absorption. In the split-window range, where solar radiation is negligible for the Earth system, (12) reduces to a simpler form

$$\begin{aligned} L(j) = {} & t_1(j)\varepsilon(j)\,\mathrm{B}(j, T_s) \\ & + \frac{1-\varepsilon(j)}{\pi}\,t_2(j)\,E_a(j) + L_a(j). \end{aligned} \tag{13}$$

IV. A Generalized Split-Window LST Algorithm

As mentioned early, the split-window method has been used by several authors for retrieving land-surface temperature. There are several major advantages of this method. It does not need profiles of atmospheric water vapor and temperature. It corrects for atmospheric effects based on the differential absorption in adjacent thermal infrared bands rather than on absolute atmospheric transmission in a single band so that it is less sensitive to the uncertainties in optical properties of the atmosphere. And it is simple and computationally efficient. We present a generalized split-window algorithm for retrieving land-surface temperature from space, specifically using NOAA-11 AVHRR data and MODIS data in the following sections.

A. View-Angle Dependent LST Algorithm

Becker and Li [19] presented a split-window LST algorithm for viewing angles up to 46° from nadir in form of

$$T_s = A_0 + P\,\frac{T_4 + T_5}{2} + M\,\frac{T_4 - T_5}{2}. \tag{14}$$

For NOAA-11 AVHRR, the coefficients are [25]

$$\begin{aligned} A_0 &= 1.274 \\ P &= 1 + 0.156\,16\,\frac{1-\varepsilon}{\varepsilon} - 0.482\,\frac{\Delta\varepsilon}{\varepsilon^2} \\ M &= 6.26 + 3.98\,\frac{1-\varepsilon}{\varepsilon} + 38.33\,\frac{\Delta\varepsilon}{\varepsilon^2} \end{aligned}$$

where $\varepsilon = 0.5(\overline{\varepsilon_4} + \overline{\varepsilon_5})$ and $\Delta\varepsilon = \overline{\varepsilon_4} - \overline{\varepsilon_5}$.

Since the maximum viewing angle for AVHRR sensors is 69° from nadir, pixels with viewing angle larger than 46° account for nearly 30% of the total pixels, or almost 50% of

the total coverage area within each swath. We have to develop a LST algorithm for the whole viewing angle range in order to provide a global coverage for LST. Although a LST algorithm in a quadratic form of combinations of μ (cosine of the viewing angle) and TIR band brightness temperatures [18] gives better accuracies in cases where surface emissivity is known, it may be sensitive to uncertainties in emissivity and noise in band radiance data caused by broken clouds of subpixel size. In the following, we use a linear form for the Wan–Dozier [18] LST algorithm

$$T_s = C + \left(A_1 + A_2\frac{1-\varepsilon}{\varepsilon} + A_3\frac{\Delta\varepsilon}{\varepsilon^2}\right)\frac{T_4+T_5}{2} + \left(B_1 + B_2\frac{1-\varepsilon}{\varepsilon} + B_3\frac{\Delta\varepsilon}{\varepsilon^2}\right)\frac{T_4-T_5}{2}. \quad (15)$$

A_1 is not fixed at 1, so there is one more variable coefficient in this form than in Becker–Li [19] algorithm. We have examined the view-angle effect by comparing the accuracies of the view-angle (θ_v) independent algorithm with the θ_v-dependent algorithm. In the θ_v-independent algorithm, coefficients are obtained by regression analysis of simulation data sampled from the whole θ_v range. In the θ_v-dependent algorithm, coefficients are obtained by regression analysis of simulation data at individual viewing angles. In the first example, we consider only cold and dry atmospheric conditions. The atmospheric lower boundary temperature, i.e., T_{air}, ranges from 256–287 K, and atmospheric vertical column water vapor (i.e., in the nadir direction) ranges from almost 0–2 cm. Fig. 2(a) shows the viewing angle dependence of the rms LST errors of the θ_v-independent and θ_v-dependent AVHRR LST algorithms for the first emissivity group with higher band emissivities. NOAA-11 AVHRR bands 4 and 5 are used in the split-window LST algorithms. Simulations show that the θ_v-independent and θ_v-dependent algorithms give almost the same maximum errors in the worst cases, which are about 3–6 times the rms errors. But the rms errors in the θ_v-dependent algorithm (shown by Xs) are much smaller than in the θ_v-independent algorithm (shown by line) at most viewing angles. Since the maximum error is larger than 4 K even in the θ_v-dependent algorithm, we tried LST iterations once and twice. In the first LST iteration, we used LST coefficients for the two subranges of $T_s - T_{\text{air}}$, one from -2 to $+16$ K, another from -16 to $+2$ K. The retrieved T_s value is used to determine which subrange should be used in the first iteration. As shown in Fig. 2(b), if the surface temperature is within its upper subrange, both rms and maximum errors can be significantly reduced. If the surface temperature is within its lower subrange, no much improvement can be made due to the small TIR signature from the surface. If we divide the T_s range into 4 subranges, the second iteration improves the LST accuracy in 3 subranges as shown in Fig. 2(c) and (d). In this way, the θ_v-dependent algorithm improves the LST accuracy by a factor from 1–3.

The θ_v-dependent LST algorithm is better than the θ_v-independent algorithms because the optical path at viewing angle 69° is more than twice the value at the nadir viewing angle. When atmospheric column water vapor is larger than 4.5 cm, the atmospheric transmission function reduces by a factor of 3 from nadir to viewing angle 69° in AVHRR band 4, and by a factor of 4 in AVHRR band 5. By using the θ_v-dependent algorithm, the variation in the atmospheric column water vapor is separated from the optical path change with viewing angle so that the accuracy is improved. The θ_v-dependent algorithm will be the only choice to retrieve LST at an accuracy of the 1 K level for the whole scan swath range.

B. Using Column Water Vapor in the θ_v-Dependent LST Algorithm

Simulations also indicate that although the rms LST error is smaller than 1 K, the maximum LST error exceeds 2 and 3.5 K at viewing angles 45 and 69°. We can further improve the LST accuracy by separating the column water vapor range into 1 or 0.5 cm intervals. The accuracy of the θ_v-independent LST algorithm is only slightly improved by using the column water vapor information, but the accuracy of the θ_v-dependent LST algorithm could be dramatically improved. With one iteration of the 1 cm-interval θ_v-dependent algorithm, the rms error does not exceed 0.7 K and the maximum error does not exceed 3 K even at the largest viewing angle. If the LST algorithm for column water vapor intervals of 0.5 cm is used, the rms error does not exceed 0.51 K and the maximum error does not exceed 1.7 K, even at viewing angle 69°. In the viewing angle range up to 45°, the rms error does not exceed 0.27 K and the maximum error does not exceed 0.91 K.

C. Using Atmospheric Lower Boundary Temperature in the θ_v-Dependent LST Algorithm

When column water vapor in a tropical atmosphere is greater than 4 cm, the atmospheric transmission functions in AVHRR bands 4 and 5 reduce to 0.22 and 0.12, respectively, and LST retrieval from satellite TIR data becomes difficult at large viewing angles. The maximum temperature deficit (defined as the difference between the surface temperature and the brightness temperature at the top of the atmosphere) in AVHRR band 4 may be as large as 27 K. In order to get a quantitative assessment of the retrieved LST accuracy, we developed two sets of θ_v-dependent algorithms for two ranges of the atmospheric lower boundary temperature, one from 300–310 K, the other from 300–305 K. The rms and maximum errors of the LST algorithm for the wider T_{air} range may be larger than 1 K and 3.8 K, respectively. The maximum LST error can be reduced by 1–2 K if the 300–305 K LST algorithm is used. Fig. 3 shows the viewing angle dependence of the rms LST errors of the θ_v-independent and θ_v-dependent MODIS LST algorithms in the wide warm atmospheric conditions (300 K $\leq T_{\text{air}} \leq$ 310 K, column water vapor 3–4 cm) for the first emissivity group. MODIS bands 31 and 32 are used in the split-window LST algorithms. The θ_v-dependent algorithm gives much smaller rms errors especially at smaller viewing zenith angles. Note that larger overlaps are used for the range of water vapor and for four subranges of the surface temperature as shown in Fig. 3 for a better stability of the algorithm. Because the nature of statistical regression method, the coefficients obtained in one range cannot be applied to outside this range. Otherwise, errors may be very large.

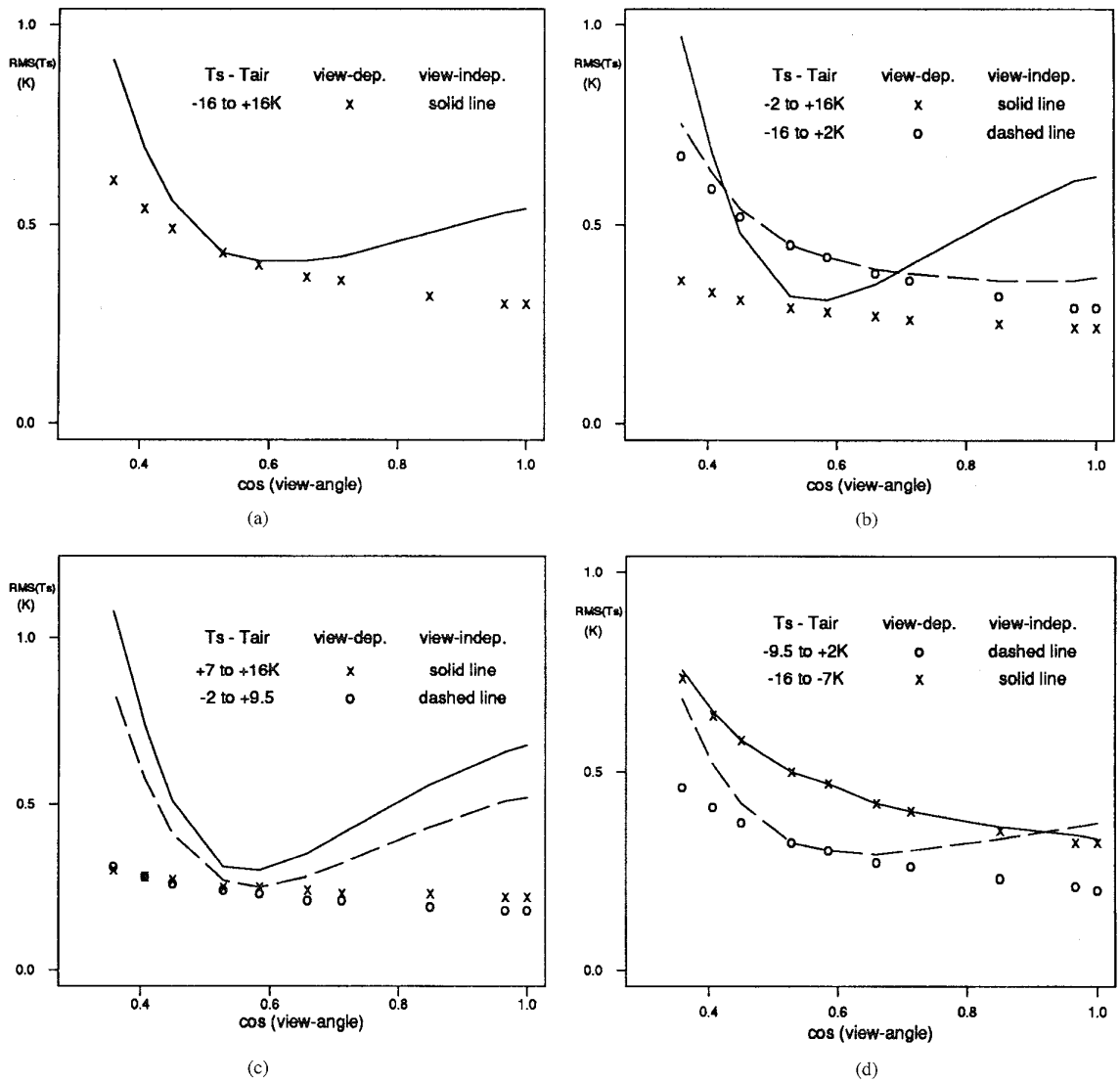

Fig. 2. Comparison between rms LST errors in θ_v-independent (shown by lines) and θ_v-dependent (shown by points) AVHRR LST algorithms in cold, dry atmospheric conditions (T_s in 256–287 K and column water vapor in 0–2 cm) for the higher emissivity group in ranges of $T_s - T_{\text{air}}$: (a) -16 to $+16$ K, (b) -16 to $+2$ K and -2 to $+16$ K, (c) -2 to $+9.5$ K and $+7$ to $+16$ K, and (d) -9.5 to $+2$ K, and -16 to -7 K.

D. Sensitivity Analysis

A better LST algorithm must have the following two features: 1) it retrieves LST more accurately; and 2) it is less sensitive to uncertainties in our knowledge of surface emissivities and atmospheric properties, and to the instrument noise. So far we have seen that the θ_v-dependent generalized split-window LST algorithm retrieves LST more accurately than θ_v-independent LST algorithms. Now we turn to the analysis of sensitivity to uncertainties in surface emissivities. According to (15), the factors on the emissivity terms $(1-\varepsilon)/\varepsilon$ and $\Delta\varepsilon/(\varepsilon^2)$ are

$$\alpha = A_2 \frac{T_4 + T_5}{2} + B_2 \frac{T_4 - T_5}{2} \tag{16}$$

and

$$\beta = A_3 \frac{T_4 + T_5}{2} + B_3 \frac{T_4 - T_5}{2}. \tag{17}$$

The view-angle dependencies of the emissivity sensitivities for these two algorithms in cold, dry atmospheric conditions ($T_{\text{air}} \leq 287.2$ K and column water vapor in 0.5–1 cm) are shown in Fig. 4. There is no significant difference in maximum α values of these two LST algorithms, but the maximum β values are very different. Max (β) values in the θ_v-independent LST algorithm are close to 160, larger than twice the values in the θ_v-dependent algorithm. This means that the θ_v-independent algorithm will have a LST error up to 1.6 K if there is an uncertainty of 0.01 in the value of $\Delta\varepsilon/(\varepsilon^2)$. We expect that this uncertainty may be around 0.005 for well known land surfaces. Then the θ_v-independent algorithm will have a 0.8 K error in the whole range of viewing angle. The θ_v-dependent algorithm is much less sensitive to the value $\Delta\varepsilon/(\varepsilon^2)$, giving a maximum LST error around 0.37 K at the nadir viewing angle.

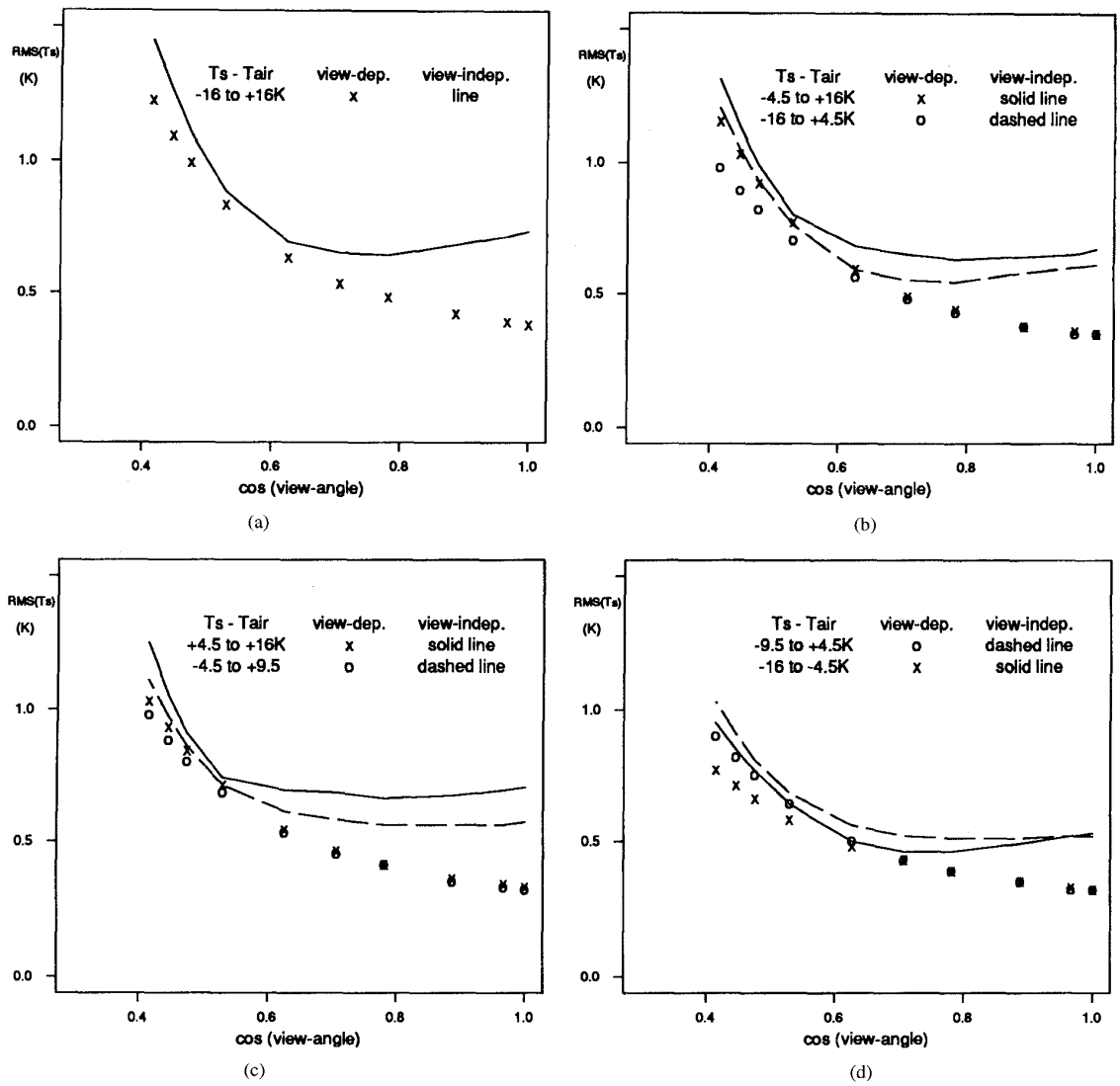

Fig. 3. Comparison between rms LST errors in θ_v-independent (shown by lines) and θ_v-dependent (shown by points) MODIS LST algorithms in warm, wet atmospheric conditions (T_s in 300–310 K and column water vapor in 3–4 cm) for the higher emissivity group in ranges of $T_s - T_{\rm air}$: (a) -16 to $+16$ K, (b) -16 to $+4.5$ K and -4.5 to $+16$ K, (c) -4.5 to $+9.5$ K and $+4.5$ to $+16$ K, and (d) -9.5 to $+4.5$ K and -16 to -4.5 K.

Fig. 5 show the maximum emissivity sensitivities in warm, dry atmospheric conditions (294 K $\leq T_{\rm air} \leq$ 300 K and column water vapor 0.5–1 cm). The maximum β value in the θ_v-independent algorithm is as large as 180, its corresponding value in θ_v-dependent algorithm is about 90 at nadir. As expected, all LST algorithms are more sensitive to uncertainty in $\Delta\varepsilon$ in dry atmospheric conditions. This sensitivity decreases as atmospheric column water vapor increases, because of the compensative effect of the reflected downward atmospheric thermal infrared radiation.

In order to investigate the sensitivity of the θ_v-dependent LST algorithm to instrument noise, we simulate the instrument noise by synthetic quantization. The radiance values of AVHRR bands 4 and 5 saturate at about 325 K. The radiance values are expressed by a 10-b integer through synthetic quantization and then converted to double precision floating point number by multiplying the quantization step. We compare the rms and maximum LST errors by applying the same θ_v-dependent algorithm to the original simulation data and the data after synthetic quantization. We change 10 bits to 9 bits and make a similar comparison. The differences in rms and maximum errors due to quantizations using 10 and 9 bits are shown in Table III, for all viewing angles up to 69°. These results show that the θ_v-dependent LST algorithm is quite stable with 10-b AVHRR data. It will be more stable with 12-b MODIS data.

V. Some Procedural Considerations

A. Programming the θ_v-Dependent LST Algorithm

Although we used a lot of computer time to establish a complete hierarchical θ_v-dependent LST algorithm, the algo-

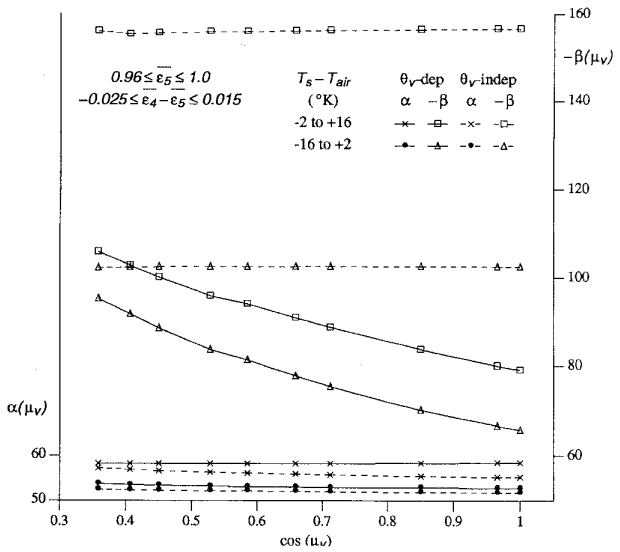

Fig. 4. The maximum sensitivities of emissivity variations in the generalized LST algorithms in relatively cold atmospheric conditions ($T_{\text{air}} \leq 287$ K and column water vapor in 0.5–1 cm).

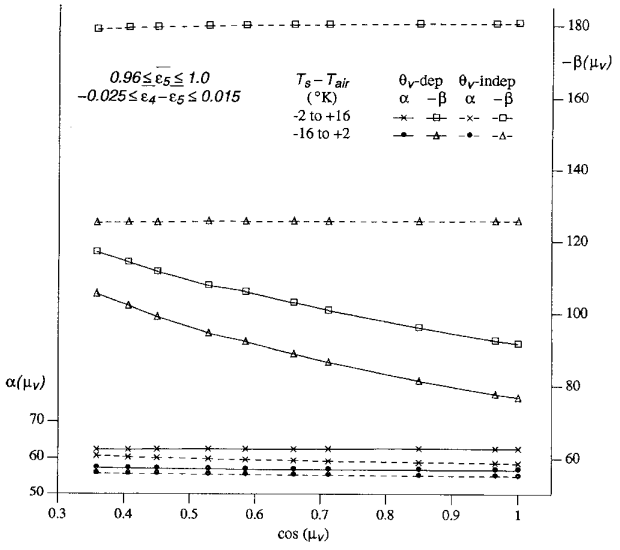

Fig. 5. The maximum sensitivities of emissivity variations in the generalized LST algorithms in warm atmospheric conditions (294 K $\leq T_{\text{air}} \leq$ 300 K and column water vapor in 0.5–1 cm).

rithm itself is simple and efficient. Once it is established, its coefficients go into a multidimensional look-up table. As shown in Fig. 6, the coefficients of the LST algorithm vary smoothly with viewing angle. Therefore, it is enough to keep in the look-up table coefficients at no more than 10 viewing angles. The coefficients at any viewing angle can be interpolated from these coefficients. The calibrated TIR band radiance data can be easily converted to band brightness temperature values by using look-up tables at an accuracy better than the sensor's NEΔT.

B. LST Production

LST production consists of the following major steps.

1) *Cloud Masking:* Cloudy pixels are detected and skipped in the LST production.
2) *Estimation of Atmospheric Column Water Vapor and Lower Boundary Temperature:* The atmospheric column water vapor and lower boundary temperature, estimated from regional and seasonal climatological data, are useful if we separate the entire simulation space into broad sub ranges [65].

   The atmospheric column water vapor and lower boundary temperature retrieved from NOAA HIRS/2 data may be used in the LST algorithm for AVHRR data. But we cannot always expect accurate column water vapor values for AVHRR pixels because HIRS/2 has a coarser spatial resolution than AVHRR and the spatial variation in atmospheric water vapor may be large.

   The θ_v-dependent LST algorithm proposed in this paper will be more suitable for MODIS data, because MODIS has almost all the channels in AVHRR and HIRS/2 at the same 1 km resolution. As shown in the previous section, the atmospheric column water vapor and lower boundary temperature retrieved from MODIS atmospheric sounding channels can significantly improve the LST accuracy, especially in wet atmospheric conditions and at large viewing angles.
3) *Land-Surface Types and Fractional Vegetation Cover:* The VNIR channels of AVHRR and MODIS can be used to estimate land-surface types and to derive the normalized differential vegetation index (NDVI). If we know that the land-surface type of a pixel is fully dense vegetation, snow/ice cover, or water surface, then the band emissivities in AVHRR bands 4 and 5, or similarly in MODIS bands 31 and 32 can be estimated through an a priori emissivity knowledge base such as shown in Fig. 1. In arid and semiarid areas, vegetation cover can be sparse and may also evolve rapidly with time. Therefore, surface emissivity may be different from one pixel to another. Kerr *et al.* [22] show that the fractional vegetation cover coefficient C may be estimated from the NDVI values with the expression

$$C = \frac{\text{NDVI} - \text{NDVI}_{\text{bs}}}{\text{NDVI}_v - \text{NDVI}_{\text{bs}}} \tag{18}$$

where NDVI_{bs} is the minimum value of the NDVI for bare soil over the area of interest and NDVI_v corresponds to the highest NDVI you can expect for a fully vegetated pixel (typically by the end of the rain season). It may be possible to estimate band emissivities of bare soils based on soil types from image classification (and soil maps if available). Finally, band emissivities can be estimated from fractional vegetation cover values pixel by pixel. Once band emissivities are known, LST can be retrieved.

TABLE III
THE MAXIMUM SENSITIVITY (KELVIN) OF THE θ_v-DEPENDENT LST ALGORITHM TO THE INSTRUMENT NOISE IN WARM ATMOSPHERIC CONDITIONS (294 K $\leq T_{\rm air} \leq$ 300 K)

application ranges		10-bit quantization		9-bit quantization	
cwv_V (cm)	$\overline{\varepsilon_5}$	$\Delta RMS(\delta T_s)$	$\Delta \max(\delta T_s)$	$\Delta RMS(\delta T_s)$	$\Delta \max(\delta T_s)$
first emissivity group ($0.96 \leq \overline{\varepsilon_5} \leq 1.0$ and $-0.025 \leq \overline{\varepsilon_4} - \overline{\varepsilon_5} \leq 0.015$)					
0 - 0.5	.96-1.0	0.07 °K	0.16 °K	0.18 °K	0.48 °K
0.5 - 1	.96-1.0	0.05 °K	0.12 °K	0.13 °K	0.35 °K
1 - 1.5	.96-1.0	0.04 °K	0.17 °K	0.12 °K	0.32 °K
1.5 - 2	.96-1.0	0.04 °K	0.15 °K	0.12 °K	0.29 °K
2 - 2.5	.96-1.0	0.05 °K	0.20 °K	0.14 °K	0.33 °K
2.5 - 3	.96-1.0	0.07 °K	0.23 °K	0.19 °K	0.49 °K
3 - 3.5	.96-1.0	0.08 °K	0.23 °K	0.23 °K	0.58 °K
second emissivity group ($0.91 \leq \overline{\varepsilon_5} \leq 0.95$ and $-0.025 \leq \overline{\varepsilon_4} - \overline{\varepsilon_5} \leq 0.015$)					
0 - 0.5	.91-.95	0.08 °K	0.28 °K	0.22 °K	0.66 °K
0.5 - 1	.91-.95	0.06 °K	0.40 °K	0.19 °K	0.62 °K
1 - 1.5	.91-.95	0.04 °K	0.30 °K	0.16 °K	0.71 °K
1.5 - 2	.91-.95	0.04 °K	0.20 °K	0.13 °K	0.56 °K
2 - 2.5	.91-.95	0.05 °K	0.21 °K	0.15 °K	0.45 °K
2.5 - 3	.91-.95	0.05 °K	0.22 °K	0.17 °K	0.57 °K
3 - 3.5	.91-.95	0.06 °K	0.30 °K	0.22 °K	0.58 °K

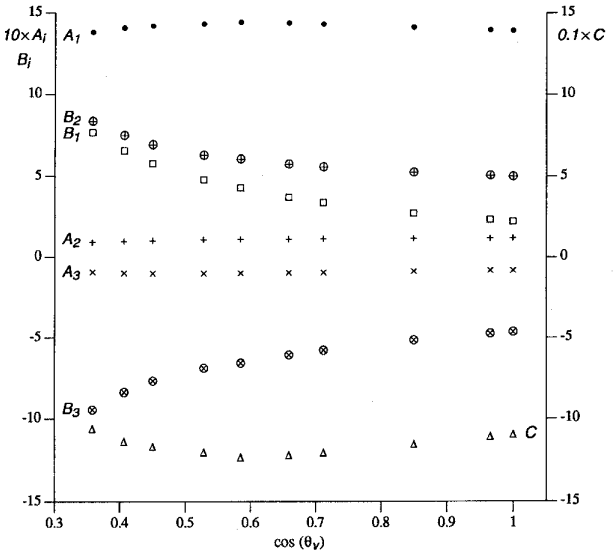

Fig. 6. The coefficients of the generalized LST algorithm for the higher emissivity group in the ranges of $T_{\rm air}$ 300–305 K, column water vapor 3.5–4 cm, and -2 K $\leq T_s - T_{\rm air} \leq$ 9.5 K.

C. Validation

We plan to validate the LST product by field measurements, airborne TIMS (thermal imaging multispectral spectrometer) and MAS (MODIS airborne simulator) data in different regions and seasons over a wide range of the atmospheric condition. This will be a multiyear effort.

VI. CONCLUSION

We propose a generalized split-window method for retrieving land-surface temperature from AVHRR and MODIS data. The coefficients of this LST algorithm depend on viewing angle. When atmospheric column water vapor increases and viewing angle is larger than 45°, it is necessary to optimize the split-window method by separating the ranges of the atmospheric column water vapor, lower boundary temperature, and surface temperature into tractable subranges. The atmospheric lower boundary temperature and (vertical) column water vapor values retrieved from HIRS/2 or MODIS atmospheric sounding channels can be used to determine the range for the optimum coefficients of the split-window method. This viewing-angle dependent algorithm not only retrieves LST more accurately, but it is also less sensitive than viewing-angle independent LST algorithms to the uncertainty in the band emissivities of the land-surface in the split-window and to the instrument noise. Validation and refinement of this new LST algorithm have been planned. The major difficulty in using this generalized split-window LST algorithm is how to assign appropriate band emissivities for each pixels in real processing. It is necessary to enhance the emissivity knowledge base of natural terrestrial materials and to develop new algorithms for simultaneously retrieving surface emissivities and temperature for land covers with variable emissivities.

VII. COEFFICIENTS AVAILABLE ELECTRONICALLY

Digital values of the coefficients of the θ_v-dependent LST algorithm can be requested via electronic mail to wan@icess.ucsb.edu.

ACKNOWLEDGMENT

The authors wish to express their gratitude to J. Salisbury at Johns Hopkins University, Baltimore, MD, for supplying spectral reflectance data, Z.-L. Li at National Center of Scientific Research, Illkirch-Graffenstaden, France, for radiosonde data, and T. Ariyama at University of Tokyo, Japan, and T. Matsunaga at Geological Survey of Japan for the thirty-year averaged quarterly atmospheric temperature and humidity profiles of Japan.

REFERENCES

[1] H. Mannstein, "Surface energy budget, surface temperature, and thermal inertia," in *Remote Sensing Applications in Meteorology and Climatology,* R. A. Vaughan and D. Reidel, Eds. Dordrecht: Netherlands, 1987 (NATO ASI Ser. C: Math. Phys. Sci., vol. 201).

[2] P. J. Sellers F. G. Hall, G. Asrar, D. E. Strebel, and R. E. Murphy, "The first ISLSCP Field Experiment (FIFE)," *J. Bull. Amer. Meteor. Soc.,* vol. 69, no. 1, pp. 22–27, 1988.

[3] T. J. Schmugge and J. C. André, Eds., *Land Surface Evaporation: Measurements and Parameterization.* New York: Springer-Verlag, 1991.

[4] S. W. Running, C. Justice, V. Salomonson, D. Hall, J. Barker, Y. Kaufman, A. Strahler, A. Huete, J.-P. Muller, V. Vanderbilt, Z. Wan, and P. Teillet, "Terrestrial remote sensing science and algorithms planned for EOS/MODIS," *J. Int. J. Remote Sensing,* vol. 15, no. 17, pp. 3587–3620, 1994.

[5] R. C. Vining and B. L. Blad, "Estimation of sensible heat flux from remotely sensed canopy temperatures," *J. Geophys. Res.,* vol. 97, no. D17, pp. 18951–18954, 1992.

[6] F. Kimura and A. P. Shimiru, "Estimation of sensible and latent heat fluxes from soil surface temperature using a linear air land heat transfer model," *J. Appl. Meteor.,* vol. 33, no. 4, pp. 477–489, 1994.

[7] G. R. Diak and M. S. Whipple, "Improvements to models and methods for evaluating the land-surface energy balance and effective roughness using radiosonde reports and satellite-measured skin temperature data," *Agricul. Forest Meteor.,* vol. 63, no. 3–4, pp. 189–218, 1993.

[8] G. A. Meehl, "Influence of the land surface in the Asian summer monsoon: external conditions versus internal feedbacks," *J. Climate,* vol. 7, pp. 1033–1049, 1994.

[9] R. D. Jackson, R. J. Reginato, and S. B. Idso, "Wheat canopy temperature: A practical tool for evaluating water requirements," *Water Resour. Res.,* vol. 13, pp. 651–656, 1977.

[10] V. Caselles and J. A. Sobrino, "Determination of frosts in orange groves from NOAA-9 AVHRR data," *Remote Sensing Environ.,* vol. 29, no. 2, pp. 135–146, 1989.

[11] A. B. Kahle, D. P. Madura, and J. M. Soha, "Middle infrared multispectral aircraft scanner data: Analysis for geological applications," *Appl. Optics,* vol. 19, pp. 2279–2290, 1980.

[12] A. B. Kahle, "Surface emittance, temperature, and thermal inertia derived from Thermal Infrared Multispectral Scanner (TIMS) data for Death Valley, California," *Geophysics,* vol. 52, no. 7, pp. 858–874, 1986.

[13] S. J. Hook, A. R. Gabell, A. A. Green, and P. S. Kealy, "A comparison of techniques for extracting emissivity information from thermal infrared data for geological studies," *Remote Sensing Environ.,* vol. 42, pp. 123–135, 1992.

[14] J. C. Price, "Estimating surface temperature from satellite thermal infrared data—A simple formulation for the atmospheric effect," *Remote Sensing Environ.,* vol. 13, pp. 353–361, 1983.

[15] J. Susskind, J. Rosenfield, D. Reuter, and M. T. Chahine, "Remote sensing of weather and climate parameters from HIRS2/MSU on TIROS-N," *J. Geophys. Res.,* vol. 89, no. D3, pp. 4677–4697, 1984.

[16] J. C. Price, "Land surface temperature measurements from the split window channels of the NOAA-7 AVHRR," *J. Geophys. Res.,* vol. 79, pp. 5039–5044, 1984.

[17] F. Becker, "The impact of spectral emissivity on the measurement of land surface temperature from a satellite," *Int. J. Remote Sensing,* vol. 8, no. 10, pp. 1509–1522, 1987.

[18] Z. Wan and J. Dozier, "Land-surface temperature measurement from space: physical principles and inverse modeling," *IEEE Trans. Geosci. Remote Sensing,* vol. 27, no. 3, pp. 268–278, 1989.

[19] F. Becker and Z.-L. Li, "Toward a local split window method over land surface," *Int. J. Remote Sensing,* vol. 3, pp. 369–393, 1990.

[20] J. A. Sobrino, C. Coll, and V. Caselles, "Atmospheric corrections for land surface temperature using AVHRR channel 4 and 5," *Remote Sensing Environ.,* vol. 38, no. 1, pp. 19–34, 1991.

[21] A. Vidal, "Atmospheric and emissivity correction of land surface temperature measured from satellite using ground measurements or satellite data," *Int. J. Remote Sensing,* vol. 12, no. 12, pp. 2449–2460, 1991.

[22] Y. H. Kerr, J. P. Lagouarde, and J. Imbernon, "Accurate land surface temperature retrieval from AVHRR data with use of an improved split window algorithm," *Remote Sensing Environ.,* vol. 41, nos. 2–3, pp. 197–209, 1992.

[23] C. Ottle and M. P. Stoll, "Effect of atmospheric absorption and surface emissivity on the determination of land temperature from infrared satellite data," *Int. J. Remote Sensing,* vol. 14, no. 10, pp. 2025–2037, 1993.

[24] A. J. Prata, "Land surface temperatures derived from the advanced very high resolution radiometer and the along-track scanning radiometer 2. Experimental results and validation of AVHRR algorithms," *J. Geophys. Res.,* vol. 99, no. D6, pp. 13 025–13 058, 1994.

[25] Z.-L. Li and F. Becker, "Feasibility of land surface temperature and emissivity determination from AVHRR data," *Remote Sensing Environ.,* vol. 43, pp. 67–85, 1993.

[26] I. J. Barton, A. M. Zavody, D. M. O'Brien, D. R. Cutten, R. W. Saunders, and D. T. Llewellyn-Jones, "Theoretical algorithms for satellite-derived sea surface temperatures," *J. Geophys. Res.* vol. 94, no. D3, pp. 3365–3375, 1989.

[27] A. R. Harris and I. M. Mason, "An extension to the split-window technique giving improved atmospheric correction and total water vapor," *Int. J. Remote Sensing,* vol. 13, no. 5, pp. 881–892, 1992.

[28] J. A. Sobrino, Z.-L. Li, and M. P. Stoll, "Impact of the atmospheric transmittance and total water vapor content in the algorithms for estimating satellite sea surface temperature," *IEEE Trans. Geosci. Remote Sensing,* vol. 31, no. 5, pp. 946–952, 1993.

[29] F. X. Kneizys, E. P. Shettle, W. O. Gallery, J. H. Chetwynd, L. W. Abreu, J. E. A. Selby, S. A. Clough, and R. W. Fenn, "Atmospheric transmittance/radiance: Computer code LOWTRAN 6," Air Force Geophys. Lab., Bedford, MA, Rep. AFGL-TR-83-0187 (NTIS AD A137796), 1983.

[30] F. X. Kneizys, E. P. Shettle, L. W. Abreu, J. H. Chetwynd, G. P. Anderson, W. O. Gallery, J. E. A. Selby, and S. A. Clough "Users guide to LOWTRAN 7," Air Force Geophys. Lab., Bedford, MA, Rep. AFGL-TR-88-0177, 1988.

[31] A. Berk, L. S. Bemstein, and D. C. Robertson, "MODTRAN: A moderate resolution model for LOWTRAN 7," Spectral Sciences, Inc., Burlington, MA, Rep. GL-TR-89-0122, 1989.

[32] K. Stamnes, S.-C. Tsay, W. Wiscombe, and K. Jayaweera, "Numerically stable algorithm for discrete-ordinate-method radiative transfer in multiple scattering and emitting layered media," *Appl. Optics,* vol. 27, no. 12, pp. 2502–2509, 1988.

[33] Z. Wan and J. Dozier, "Effects of temperature-dependent molecular absorption coefficients on the thermal infrared remote sensing of the earth surface," in *Proc. IGARSS'92,* May 26–29, 1992, pp. 1242–1245.

[34] W. B. Grant, "Water vapor absorption coefficients in the 8–13-μm spectral region: A critical review," *Appl. Opt.,* vol. 29, no. 4, pp. 451–462, 1990.

[35] Q. Ma and R. Tipping, "A far wing line shape theory and its application to the foreign-broadened water vapor continuum absorption .3," *J. Chem. Phys.,* vol. 97, pp. 818–828, 1992.

[36] ——, "The detailed balance requirement and general empirical formalisms for continuum absorption," *J. Quant. Spectrosc. Radiat. Transfer,* vol. 51, pp. 751–757, 1994.

[37] S. A. Clough, F. X. Kneizys, and R. W. Davies, "Line shape and the water vapor continuum," *Atmos. Res.,* vol. 23, pp. 229–241, 1989.

[38] I. J. Barton, "Infrared continuum water vapor absorption coefficients derived from satellite data," *Appl. Opt.,* vol. 30, no. 21, pp. 2929–2934, 1991.

[39] M. J. McFarland, R. L. Miller, and C. M. U. Neale, "Land surface temperature derived from the SSM/I passive microwave brightness temperatures," *IEEE Trans. Geosci. Remote Sensing,* vol. 28, no. 5, pp. 839–845, 1990.

[40] T. J. Schmugge, P. E. O'Neill, and P. E. Wang, "Passive microwave soil moisture research," *IEEE Trans. Geosci. Remote Sensing,* vol. GRS-24, pp. 12–22, 1986.

[41] T. J. Jackson and T. J. Schmugge, "Passive microwave remote sensing of soil moisture," *Adv. Hydrosci.,* vol. 14, pp. 123–159, 1986.

[42] J. P. Wigneron, Y. Kerr, A. Chanzy, and Y. Q. Jin, "Inversion of surface parameters from passive microwave measurements over a soybean field," *Remote Sensing Environ.,* vol. 46, pp. 61–72, 1993.

[43] T. J. Jackson and P. E. O'Neill, "Salinity effects on the microwave emission of soil," *IEEE Trans. Geosci. Remote Sensing,* vol. GRS-25, pp. 214–220, 1987.

[44] V. Salomonson, W. Barnes, P. Maymon, H. Montgomery, and H. Ostrow, "MODIS: Advanced facility instrument for studies of the earth as a system," *IEEE Trans. Geosci. Remote Sensing,* vol. 27, no. 2, pp. 145–153, 1989.
[45] M. D. King, Y. J. Kaufman, W. P. Menzel, and D. Tanré, "Remote sensing of cloud, aerosol, and water vapor properties from the Moderate Resolution Imaging Spectrometer (MODIS)," *IEEE Trans. Geosci. Remote Sensing,* vol. 30, no. 1, pp. 2–27, 1992.
[46] R. A. Sutherland, "Broadband and spectral (2–18 μm) emissivity of some natural soils and vegetation," *J. Atmos. Ocean. Technol.,* vol. 3, pp. 199–202, 1986.
[47] J. W. Salisbury and D. M. D'Aria, "Emissivity of terrestrial materials in the 8–14 μm atmospheric window," *Remote Sensing Environ.,* vol. 42, pp. 83–106, 1992.
[48] M. Griggs, "Emissivities of natural surfaces in the 8- to 14-micron spectral region," *J. Geophys. Res.,* vol. 73, pp. 7545–7551, 1968.
[49] F. Nerry, J. Labed, and M. P. Stoll, "Spectral properties of land surfaces in the thermal infrared, 1, Laboratory measurements of absolute spectral emissivity signatures," *J. Geophys. Res.,* vol. 95, no. B5, pp. 7027–7044, 1990.
[50] W. G. Rees, "Infrared emissivities of Arctic land cover types," *Int. J. Remote Sensing,* vol. 14, pp. 1013–1017, 1993.
[51] J. Dozier and S. G. Warren, "Effect of viewing angle on the infrared brightness temperature of snow," *Water Resour. Res.,* vol. 18, no. 5, pp. 1424–1434, 1982.
[52] J. Labed and M. P. Stoll, "Angular variation of land surface spectral emissivity in the thermal infrared: Laboratory investigations on bare soils," *Int. J. Remote Sensing,* vol. 12, no. 11, pp. 2299–2310, 1991.
[53] W. G. Rees and S. P. James, "Angular variation of the infrared emissivity of ice and water surfaces," *Int. J. Remote Sensing,* vol. 13, pp. 2873–2886, 1992.
[54] J. W. Salisbury and D. M. D'Aria, "Infrared (8–14 μm) remote sensing of soil particle size," *Remote Sensing Environ.,* vol. 42, pp. 157–165, 1992.
[55] B. Rivard, S. B. Petroy, and J. R. Miller, "Measured effects of desert varnish on mid-infrared spectra of weathered rocks as an aid to TIMS imagery interpretation," *IEEE Trans. Geosci. Remote Sensing,* vol. 31, no. 1, pp. 284–291, 1993.
[56] L. M. Hanssen, "Effects of restricting the detector field of view when using integrating spheres," *Appl. Opt.,* vol. 28, no. 11, pp. 2097–2103, 1989.
[57] D. S. Kimes, "Azimuthal radiometric temperature measurements of wheat canopies," *Appl. Opt.,* vol. 20, no. 7, pp. 1119–1121, 1981.
[58] F. Palluconi, A. B. Kahle, G. Hoover, and J. E. Conel, "The spectral emissivity of prairie and pasture grasses at Konza Prairie, Kansas," in *Symp. FIFE,* Amer. Meteorol. Soc., Boston, MA, pp. 77–78, 1990.
[59] I. P. Grant and G. E. Hunt, "Discrete space theory of radiative transfer, I, Fundamentals," in *Proc. Royal Soc. London,* vol. A313, pp. 183–197, 1969.
[60] W. J. Wiscombe, "Extension of the doubling method to inhomogeneous sources," *J. Quant. Spectros. Radiat. Transfer,* vol. 16, no. 6, pp. 477–486, 1976.
[61] S. Li, Z. Wan, and J. Dozier, "A component decomposition model for evaluating atmospheric effects in remote sensing," *J. Electromag. Waves Applic.,* vol. 1, no. 4, pp. 323–347, 1987.
[62] K. Stamnes and P. Conklin, "A new multi-layer discrete ordinate approach to radiative transfer in vertically inhomogeneous atmospheres," *J. Quant. Spectrosc. Radiat. Transfer,* vol. 31, pp. 273–282, 1984.
[63] W. J. Wiscombe and J. W. Evans, "Exponential-sum fitting of radiative transmission functions," *J. Comput. Phys.,* vol. 24, no. 4, pp. 416–444, 1977.
[64] Z. Wan and J. Dozier, "Effects of the atmosphere and surface emissivity on the thermal infrared spectral signature measured from MODIS-N," in *Proc. IGARSS'90,* 1990, pp. 189–192.
[65] J. Dozier and Z. Wan, "Development of practical multiband algorithms for estimating land-surface temperature from EOS/MODIS data," *Adv. Space Res.,* vol. 13, no. 3, pp. 81–90, 1994.

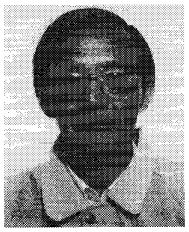

Zhengming Wan received the B.A. degree from the University of Science and Technology of China in 1965 and the Ph.D. degree from the University of California, Santa Barbara, in 1985.

He is an Associate Researcher at the University of California, Santa Barbara. He is a member of the MODIS Science Team and a Principal Investigator in NASA's Earth Observing System (EOS), and a Guest Computational Investigator in NASA's High Performance Computing and Communications Science Team. His main research activities are in radiative transfer simulation and modeling of the Earth system, and applications of remote sensing techniques.

Jeff Dozier (A'84) received the B.A. degree from California State University, Hayward, in 1968, and the Ph.D. degree from the University of Michigan, Ann Arbor, in 1973.

He is a Principal Investigator on an interdisciplinary grant in NASA's Earth Observing System (EOS), in which he and his colleagues study hydrology and hydrochemistry in the Earth's alpine areas, and he is Coprincipal Investigator of the University of California's EOSDIS project, that seeks to develop a next-generation distributed information system. He is currenly the Dean of the new School of Environmental Science and Management at the University of California, Santa Barbara. From 1990–1992, he served as the EOS Senior Project Scientist.

Dr. Dozier is a fellow of the American Geophysical Union and a Distinguished Visiting Scientist at the Jet Propulsion Laboratory. He is a member of the Computer Science and Telecommunications Board of the National Academy of Science. In 1993, he received the NASA Public Service Medal.